6. Optically Ionized Gases: Long- and Short-Lived Electrons

This chapter presents the first application of the THz spectrometer driven by the amplified laser: The intense pulses of this laser system are used to ionize various gases. The THz signal of the resulting gas plasma is dominated by the Drude response of the quasifree electrons and yields the dynamics of their density and Drude collision rate. The electron decay in Ar is found to be much slower than in O_2 due to a lack of internal dissipation channels for the electron energy. However, it can be accelerated enormously by adding the electron scavenger SF_6 to Ar. The Drude collision (or current-relaxation) rate decreases monotonously with the decaying electron density. We discuss 2 possible scenarios which can account for this behavior: The 1st scenario assumes that electron-ion scattering is the dominating mechanism for the current relaxation whereas the 2nd favors electron-electron scattering.

Parts of this chapter have been submitted to Physical Review Letters and Chemical Physics Letters.

6.1. Motivation

Free charge carriers in gases play an important role in everyday life, for example in fluorescence tubes, lightnings during a thunderstorm, and sparks in electrical equipment.

- Sparks in high-voltage devices can lead to short-circuits of the device and material corrosion. In order to prevent or interrupt such short-circuits, the devices are flooded with insulating gases such as the electron scavenger SF_6 [Chr00]. To date, the decay of free electrons in the presence of SF_6 has not been observed on an ultrashort time scale.
- It has been a longstanding dream to trigger lightnings in a thunderstorm in a controlled way [Zha95]. In this context, laser pulses are suggested to produce a channel of ionized air between the ground and the clouds which should lead to a controlled discharge of the clouds along that channel. As shown in Fig. 6.1, the potential of this scheme has been demonstrated in laboratory over distances of few meters [Kas03]. In order to cover much larger distances, knowledge on the lifetime and mobility of the induced quasifree electrons is highly desirable.

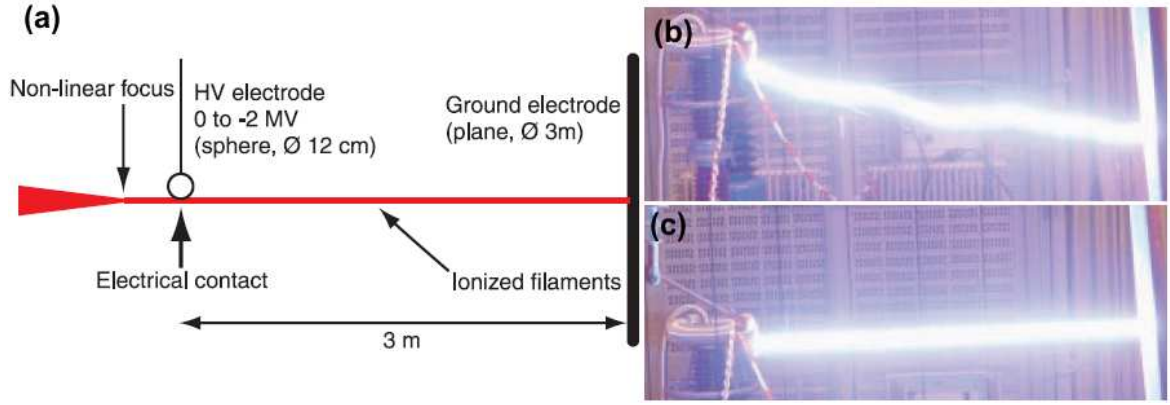

Figure 6.1.: High-voltage discharge controlled by femtosecond-laser pulses. (a) Schematic of the experimental setup. A voltage of up to 2 MV is generated between the 2 electrodes having a distance of 3 m. (b) Free discharge along an erratic path. (c) Straight discharge along a filament of ionized air generated by an intense laser pulse. This figure was taken from Ref. [Kas03].

Femtosecond time-resolved studies of gas plasmas employ powerful and short laser pulses to ionize a gas such as air. Several methods have been used to probe the free-electron dynamics of the plasma. One of these schemes involves the interferometrical or diffractive measurement of the phase shift a visible probe pulse accumulates by transmitting the plasma at a certain time after generation [Fon99, Tzo00]. In principle, this method yields the electron density n_e. However, according to the linearized Drude formula (1.18), the electron collision rate Γ is much more difficult to obtain since absorption effects are weaker than phase-shift effects by a factor $\Gamma/\omega \sim 10^{-2}$ for visible probe radiation of frequency ω. Another possibility is to detect the total light emission of a plasma that was reexcited by a delayed probe pulse [Mar04]. However, this approach is quite indirect since the functional relation between emitted light intensity and plasma quantities such as n_e is not known.

THz radiation is a promising alternative probe because Γ and the plasma frequency of optically ionized gases lie in the THz range. For example, the plasma frequency Ω_{pl} of a plasma consisting of electrons and singly ionized molecules with a number density of ambient air is $\Omega_{pl}/2\pi = 45$ THz according to Eq. (1.13). THz spectroscopy has already proven useful to characterize a He discharge plasma on a μs-time scale [Jam03] or to study the mechanism of oxygen ionization by femtosecond laser pulses [Mic05]. However, these reports investigated only a single gas in the frequency range from 1 to 3 THz and did not cover its decay dynamics comprehensively.

6.2. Partially Ionized Gases and Plasmas

In our work, laser pulses are used to ionize a fraction of the atoms or molecules in a gas. Such a partially ionized gas is also called a *plasma* when the effective interaction length λ_D of 2 charged particles is much smaller than the linear dimensions of the system under

consideration [Hol65]. Such effective interaction between "test charges" q_1 and q_2 is due to the screening of the bare Coulomb force by the surrounding electrons or ions and can often be written as an exponentially damped Coulomb potential

$$V_{q_1 q_2}(\boldsymbol{x}_1, \boldsymbol{x}_2) = \frac{q_1 q_2}{|\boldsymbol{x}_1 - \boldsymbol{x}_2|} \exp\left(-\frac{|\boldsymbol{x}_1 - \boldsymbol{x}_2|}{\lambda_\mathrm{D}}\right). \tag{6.1}$$

In a nondegenerate plasma with electron density n_e and electron temperature T_e, the screening length is the Debye length [Hol65]

$$\lambda_\mathrm{D} = \sqrt{\frac{k_\mathrm{B} T_\mathrm{e}}{4\pi e^2 n_\mathrm{e}^2}}$$

which represents a special case of the Thomas-Fermi screening length in solid-state physics. Note that Eq. (6.1) quantifies the screening of a static charge; dynamic screening may be different and is described for example by the Lindhard dielectric function [Ash76].

Further important plasma parameters are

$$\Theta = \frac{k_\mathrm{B} T_\mathrm{e}}{\epsilon_\mathrm{F}} = \frac{2 m_\mathrm{e} k_\mathrm{B} T_\mathrm{e}}{\hbar^2 (3\pi^2 n_\mathrm{e})^{2/3}} \quad \text{and} \quad G_\mathrm{ee} = \frac{Z e^2}{a k_\mathrm{B} T_\mathrm{e}},$$

where $a = (4\pi n_e/3)^{-1/3}$ is the "electron-sphere radius" [Sty02]. An electron-degeneracy parameter of $\Theta \gg 1$ indicates that the Fermi energy ϵ_F of the quasifree electrons is much smaller than their thermal energy such that the electrons can be described by Maxwell-Boltzmann statistics. In the opposite case, exchange effects become important which requires Fermi-Dirac statistics. The electron-coupling parameter G_ee quantifies the coupling strength between the electrons, and $G_\mathrm{ee} < 0.1$ indicates that the electron-electron interaction can be considered as a small perturbation of the free-electron gas [Ger05].

6.3. Dynamics of Optically Ionized Gases

As mentioned in Section 1.1, the electron dynamics in ionized gases is in principle quite similar to that in metals. However, the generation of the free electrons in gases requires intense laser pulses which ionize the atoms and molecules by promoting the electron with the lowest binding energy W_b to an unbound or "free" state. W_b is also called ionization energy. An important parameter for the description of the ionization process is the Keldysh parameter [Bra00]

$$\gamma_\mathrm{K} = \frac{\omega \sqrt{2 m_\mathrm{e} W_\mathrm{b}}}{e|E_0|}. \tag{6.2}$$

γ_K^2 can be interpreted as the ratio of the electron binding energy W_b and the peak kinetic energy $m_\mathrm{e} v_\mathrm{max}^2/2$ a *free* electron would acquire in a laser field of amplitude E_0 and frequency ω due to acceleration to a peak velocity $v_\mathrm{max} = e|E_0|/m_\mathrm{e}\omega$.

For $\gamma_K \gg 1$, the ionization can be described by multiphoton absorption based on higher-order perturbation theory [Bra00] which results, for example, in the perturbation series (1.9). On the other hand, for $\gamma_K \approx 1$ and linearly polarized light, the laser field starts to lower the Coulomb potential of the nucleus such that the electron with the binding energy W_b can tunnel through the reduced Coulomb barrier. At even higher laser fields, $\gamma_K \ll 1$, the Coulomb barrier is so low that the electron can escape classically [Pos04]. At our pump photon energy of $\hbar\omega = 1.6\,\mathrm{eV}$, the crossover region with $\gamma_K \approx 1$ is reached at laser intensities of $10^{14}\,\mathrm{W\,cm^{-2}}$.

After generation of the quasifree electrons, electron-electron scattering leads to a thermalization of the electronic system on a subpicosecond-time scale [Ger05]. Electron cooling occurs via energy transfer from the electronic system with temperature T_e to the ions described by temperature T_i. If there is only one sort of singly charged ions of mass m_i the inverse time constant of this process is given by the Spitzer formula [Spi56]

$$\frac{1}{\tau_{ei}} = \frac{3 m_e m_i}{8\sqrt{2\pi} n_i e^4 \Lambda_C} \left(\frac{k_B T_e}{m_e} + \frac{k_B T_i}{m_i} \right)^{3/2}.$$

Here, the electron-ion interaction comes into play via the so-called Coulomb logarithm $\Lambda_C = \ln(12\pi n_e \lambda_D^3)$. The Spitzer formula can be considered as an analog of the equations of the 2-temperature model in solids, see Section 1.3.2. Cooling by heat transfer to the neutral particles is usually substantially slower especially in noble gases due to the much smaller cross section for scattering between the electrons and neutral particles [Ger05].

Finally, the recombination of an electron and an ion requires a sink for the binding and the kinetic energy of the electron which is, for example, provided by internal excitations of the ion or a 3rd particle like another electron or an emitted photon. The great variety of reactions between the plasma constituents leads to a complete "zoo" of recombination reactions. It is one of the tasks of plasma physics to determine the weight of the possible reaction channels in the plasma investigated [Hol65].

6.4. Optical Properties of a Plasma

A plasma consists of quasifree electrons, ions, and neutral particles. Due to their small mass, the motion of the free electrons is expected to make the dominating contribution to the optical properties.

In the simplest approach, one can use the Drude model of Section 1.5.1 to describe the dielectric function ε of a plasma. Note that according to Eq. (1.12), $\mathrm{Re}\,\varepsilon$ becomes negative for frequencies ω below the plasma frequency Ω_{pl} which makes the plasma highly reflecting. When, in addition, the penetration depth of the electromagnetic wave into the plasma is smaller than the mean free path of an electron, the anomalous skin effect becomes operative [Ich73]. As a consequence, the electrons can create a *nonlocal* coherent polarization in plasma regions deeper than the penetration depth. However, this regime is not important

gas	Ar	O_2	SF_6	gas mixture	$0.9\,Ar + 0.1\,SF_6$
W_b (eV)	15.8	12.1	15.3	W_b (eV)	-
purity (%)	99.998	99.9	99.99	Ar content (%)	90 ± 2

Table 6.1.: Ionization energy W_b and purity of the gases investigated. As to the gas mixture $0.9\,Ar + 0.1\,SF_6$, the coefficients represent the volume fractions of the constituting gases. The values for W_b are taken from Ref. [oS05].

in the work presented here since the probe frequencies used are always above the plasma frequency resulting in a penetration depth much larger than the plasma thickness.

The Boltzmann approach of Section 1.5.2 gives a more sophisticated description of the dielectric function of a weakly coupled plasma [Sty02]. As shown later it also leads to a Drude-like dielectric function but relates the Drude collison rate Γ to microscopic quantities such as the momentum-transfer cross sections for the scattering of electrons with ions or neutral particles.

6.5. Experimental and Technical Details

The optical ionization of gases requires large light intensities. Therefore, the measurements of this chapter require light pulses from the amplified laser system which is described in Section 3.1.2.

6.5.1. Sample

All gases are obtained from Linde and Aldrich in high-pressure bottles; their purity and ionization potential W_b are listed in Table 6.1. The setup for the sample preparation consists of a gas cell which is connected to a gas bottle with a pressure regulator in-between. In order to always guarantee a fresh sample, the gas enters the gas cell at a pressure slightly above the ambient pressure of 1 bar which is the pressure at the cell outlet.

6.5.2. Sample Pumping and Probing

The gas cell is placed in the standard sample position of Fig. 3.3, but a modified pump geometry is used here: As shown in Fig. 6.2, the visible and linearly polarized pump pulse enters the gas cell through a glass window. Before, the beam is focused by 2 cylindrical lenses whose symmetry planes are perpendicular to each other leading to an elliptical beam cross section. The gas is ionized around the focal plane of lens 2 where the intensity is highest; Fig. 6.3(a) shows that the beam cross section at this position is a strongly elongated ellipse.

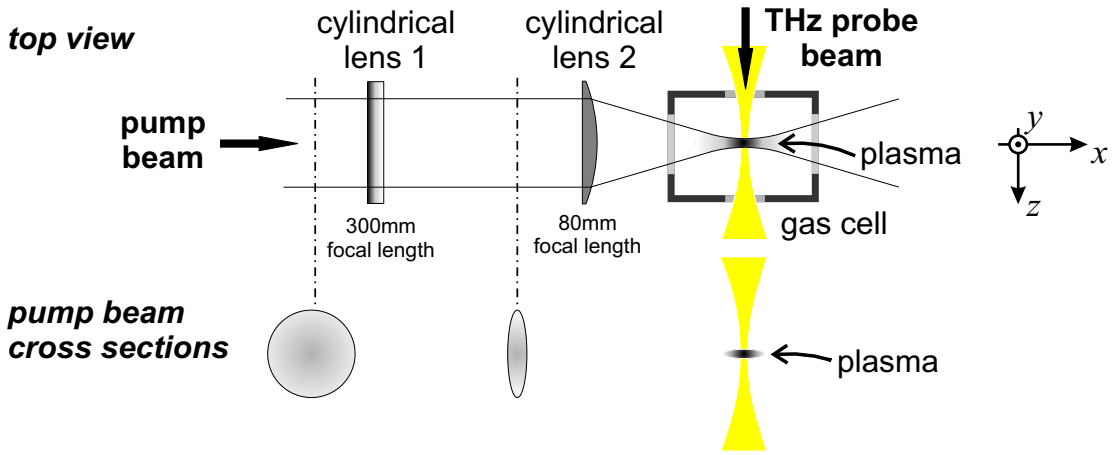

Figure 6.2.: Schematic of the sample geometry. The pump beam is focused into the gas cell by two cylindrical lenses. The resulting plasma sheet around the focal plane of lens 2 is probed by a THz beam propagating perpendicularly to the pump beam.

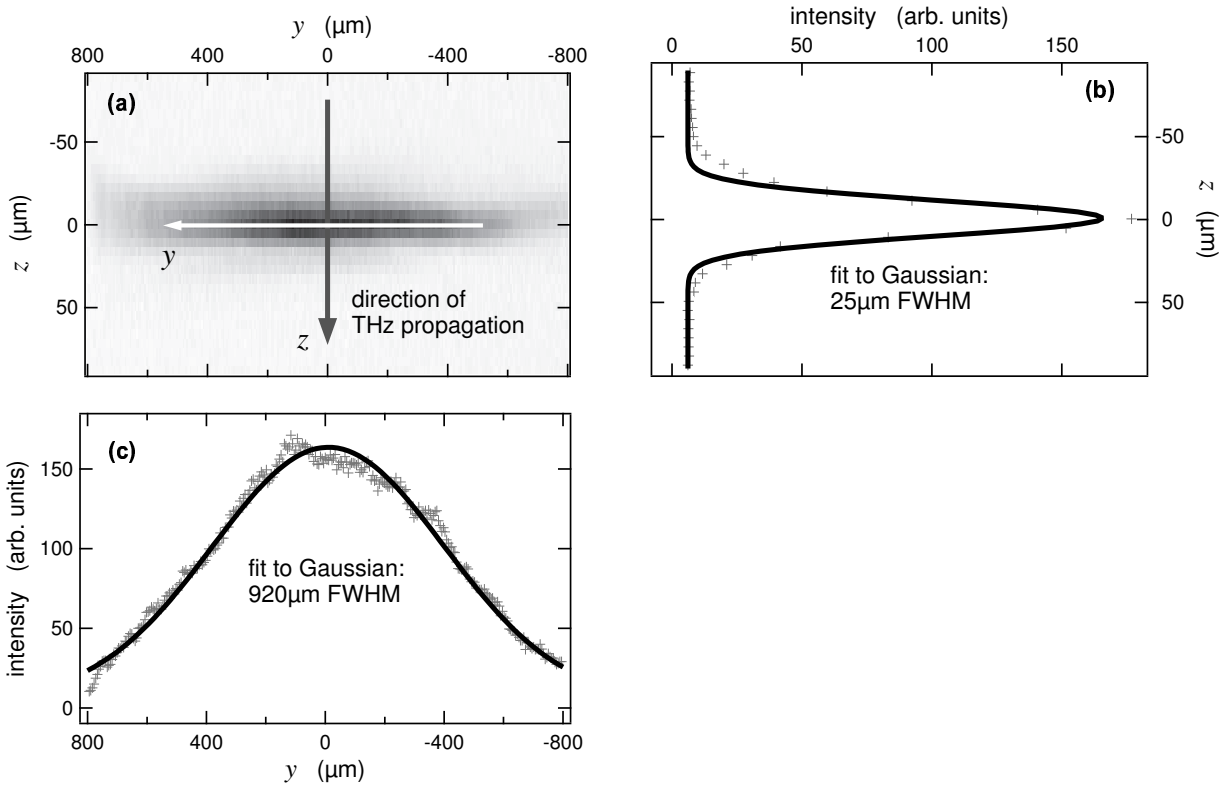

Figure 6.3.: (a) Gray-scale plot of the intensity profile I of the pump-beam focus acquired by a charge-coupled device (CCD). The THz probe pulse propagates along the z axis. Note the different axis scaling. (b) Line plot along the z direction. Here, the full width at half maximum (FWHM) of the intensity profile comes close to the CCD-pixel size of 5.5 μm. (c) Line plot along the y direction. It shows that there is nearly no intensity variation around the maximum in this direction such that the THz probe pulse sees a homogeneously excited sample perpendicular to its direction of propagation.

The THz probe beam travels in a direction perpendicular to that of the pump beam, enters the gas cell through a silicon window, transmits the plasma, and leaves the cell through another silicon window. Note that the THz probe pulse sees a homogenously excited gas *perpendicular* to its propagation direction z: As shown by Fig. 6.3(c), the pump intensity I along the y axis is nearly constant over the 50-μm diameter of the probe-beam focus. The same holds true along the x direction where the focal length of the pump focus is at least $400\,\mu$m.

However, as seen in Fig. 4.12(c), I varies strongly *along* the propagation direction z of the probe pulse and can be described by a Gaussian

$$I(z) = I(0)\,\exp\left(-4\ln 2\frac{z^2}{\mathrm{FWHM}^2}\right) \tag{6.3}$$

with a full width at half maximum of $\mathrm{FWHM} = 25\,\mu$m.

For the largest pump-pulse energies of 0.4 mJ we estimate a peak intensity of $3{\cdot}10^{13}\,\mathrm{W\,cm^{-2}}$ in the center of the focus. With a pump-photon energy of 1.6 eV, this corresponds to a Keldysh parameter (6.2) of $\gamma_\mathrm{K} \approx 15$ indicating that the regime of field ionization is not yet completely reached. In addition, we can exclude double ionization which comes into play at much higher intensities around $10^{18}\,\mathrm{W\,cm^{-2}}$ [Pos04].

The pulse shaper in the amplified laser system is employed to maximize the bandwidth of the THz pulses and the plasma-induced signal. We made sure that the latter did *not* depend on the THz intensity showing that the THz pulse can be still considered as a linear probe despite its high electric fields, see Section 3.2.4. Our temporal resolution of about 200 fs is estimated by the rise of the pump-induced signal. It is limited by the 90° beam geometry since different sample positions along the x direction in Fig. 6.2 are excited at different times.

6.5.3. Data Analysis

Unexcited Sample

Since the gas cell and its Si windows are thick, multiple reflections do not play a role in the detection window of the THz pulse, and the THz electric field propagating along the z axis through the gas long after or before excitation is

$$E_\infty(z,\omega) = E_\mathrm{inc}\exp\frac{\mathrm{i}\omega\sqrt{\varepsilon}z}{c}.$$

In this way, the dielectric function ε of SF_6 in the THz range can be measured where Ar of O_2 serve as the reference with $\varepsilon = 1$. The result is shown in Fig. 6.4 where a peak in $\mathrm{Im}\,\varepsilon$ at about 18 THz is due to the ν_4 vibration of the SF_6 molecule [Her66].

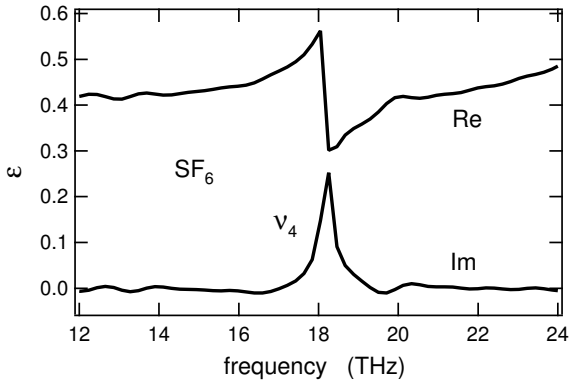

Figure 6.4.: Dielectric function of an SF_6 between 12 and 24 THz under normal conditions. Note the distinct peak in the imaginary part at about 18 THz. It originates from the ν_4 vibration of the SF_6 molecule [Her66]. The real part is offset for clarity.

Excited Sample

Exciting the sample with a pump pulse creates a change $\Delta\varepsilon_\tau$ in the dielectric function of the gas which is seen by the probe pulse at time τ after excitation. Concerning the extraction of $\Delta\varepsilon_\tau$, we are confronted with several problems: As suggested by the intensity profile of the pump-beam focus in Fig. 6.3(b), $\Delta\varepsilon_\tau(z,\omega)$ varies along the propagation direction z of the THz probe pulse. Moreover, Fig. 3.5(b) shows that the measured pump-induced changes ΔS_τ in the THz signal are too large to justify a linear relationship like Eq. (2.15) between ΔS_τ and $\Delta\varepsilon_\tau$.

However, since the dynamics after sample excitation takes place on a time scale of at least 10 ps, a quasistatic approach to the data analysis is justified. Therefore, we use the WKB approximation (2.19) to calculate the transmitted THz field at a point z_1 *after* the ionized region. The relative change in the THz field referenced to the unexcited sample is then

$$Q_\tau(\omega) = \frac{S_\tau(\omega)}{S_\infty(\omega)} = \frac{E_\tau(z_1,\omega)}{E_\infty(z_1,\omega)} = \exp\left[\mathrm{i}\frac{\omega}{c}\int_{-\infty}^{z_1}\mathrm{d}z\,\Delta n_\tau(z,\omega)\right] \tag{6.4}$$

with $\Delta n_\tau = \sqrt{1+\Delta\varepsilon_\tau} - 1$ being the pump-induced change in the refractive index.

The quality of this approximation is checked by numerically solving the wave equation (2.18) for a large variety of test functions $\Delta\varepsilon_\tau$. The numerical procedure involves the summation of the perturbation series (2.5) up to the 100th order or more until convergence is achieved. The agreement between this solution and Eq. (6.4) is excellent even for spatially narrow profiles of $\Delta\varepsilon_\tau$ where the WKB approximation is expected to fail.

How can one deal with the unknown spatial variation of the dielectric function? In contrast to the measurements on graphite and carbon nanotubes, $\Delta\varepsilon_\tau(z,\omega)$ does not follow the intensity profile $I(z)$ of the pump beam. Here, we assume a power law for the change in the refractive index with respect to the pump intensity,

$$\frac{\mathrm{Re}\,\Delta n(z,\omega)}{\mathrm{Re}\,\Delta n(0,\omega)} = \left[\frac{I(z)}{I(0)}\right]^{p_{\mathrm{Re}}} \quad \text{and} \quad \frac{\mathrm{Im}\,\Delta n(z,\omega)}{\mathrm{Im}\,\Delta n(0,\omega)} = \left[\frac{I(z)}{I(0)}\right]^{p_{\mathrm{Im}}}. \tag{6.5}$$

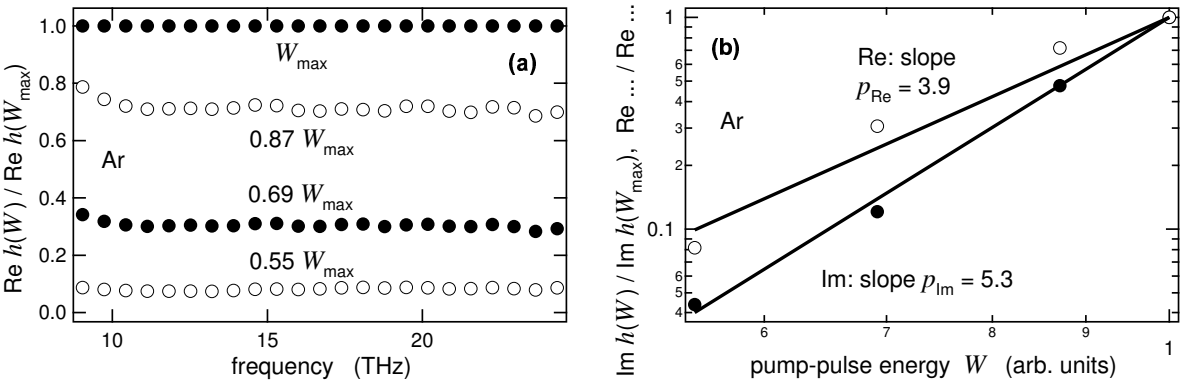

Figure 6.5.: (a) Spectral dependence of the auxiliary quantity h of Eq. (6.6) measured in Ar 5 ps after excitation with different pump-pulse energies W. The reference pulse energy of $W_{\max} = 0.4\,\mathrm{mJ}$ corresponds to a maximum intensity of $I(z=0) \approx 3 \cdot 10^{13}\,\mathrm{W\,cm^{-2}}$ in the center of the pump focus. (b) Dependence of the spectrally averaged h on the pump intensity together with fits to a power law.

As a consequence, real and imaginary part of the auxiliary quantity

$$h(W) := -\mathrm{i}\,\ln Q_\tau = \frac{\omega}{c}\int_{-\infty}^{z_0} \mathrm{d}z\,\Delta n_\tau(z,\omega) \tag{6.6}$$

should obey the corresponding power law with respect to the pump pulse energy W,

$$\frac{\mathrm{Re}\,h(W)}{\mathrm{Re}\,h(W_{\max})} = \left(\frac{W}{W_{\max}}\right)^{p_{\mathrm{Re}}} \quad \text{and} \quad \frac{\mathrm{Im}\,h(W)}{\mathrm{Im}\,h(W_{\max})} = \left(\frac{W}{W_{\max}}\right)^{p_{\mathrm{Im}}}. \tag{6.7}$$

Indeed, as seen in Fig. 6.5(a) for Ar at $\tau = 5\,\mathrm{ps}$ after excitation, the left-hand sides of both equations (6.7) do *not* depend on frequency. Moreover, Fig. 6.5(b) shows that they can be adequately described by a power law with exponents $p_{\mathrm{Re}} = 3.9$ and $p_{\mathrm{Im}} = 5.3$, respectively. We conclude that the ansatz (6.5) for the spectral shape of the pump-induced change Δn_τ in the refractive index is reasonable. For O_2, we find exponents of $p_{\mathrm{Re}} = 2.9$ and $p_{\mathrm{Im}} = 4.5$; the exponents for SF_6 are assumed to agree with those of Ar because of the similar ionization potential.

We now employ Eqs. (6.3), (6.6), and (6.5) to obtain

$$\mathrm{Re}\,(\mathrm{i}\,\ln Q_\tau) = -\frac{\omega}{c}\frac{\mathrm{FWHM}}{\sqrt{0.88 p_{\mathrm{Re}}}}\,\mathrm{Re}\,\Delta n_\tau(z=0,\omega) \tag{6.8}$$

and an analog expression for the imaginary part which both allow for the extraction of the dielectric function $1 + \Delta\varepsilon_\tau(z=0,\omega)$ in the center of the pump-induced plasma.

We assume that the ansatz (6.5) is still valid at longer delays τ. This assumption is justified since transport effects are not expected to play an important role during the first 200 ps after plasma generation according to Ref. [Dun94]. They measured the expansion of

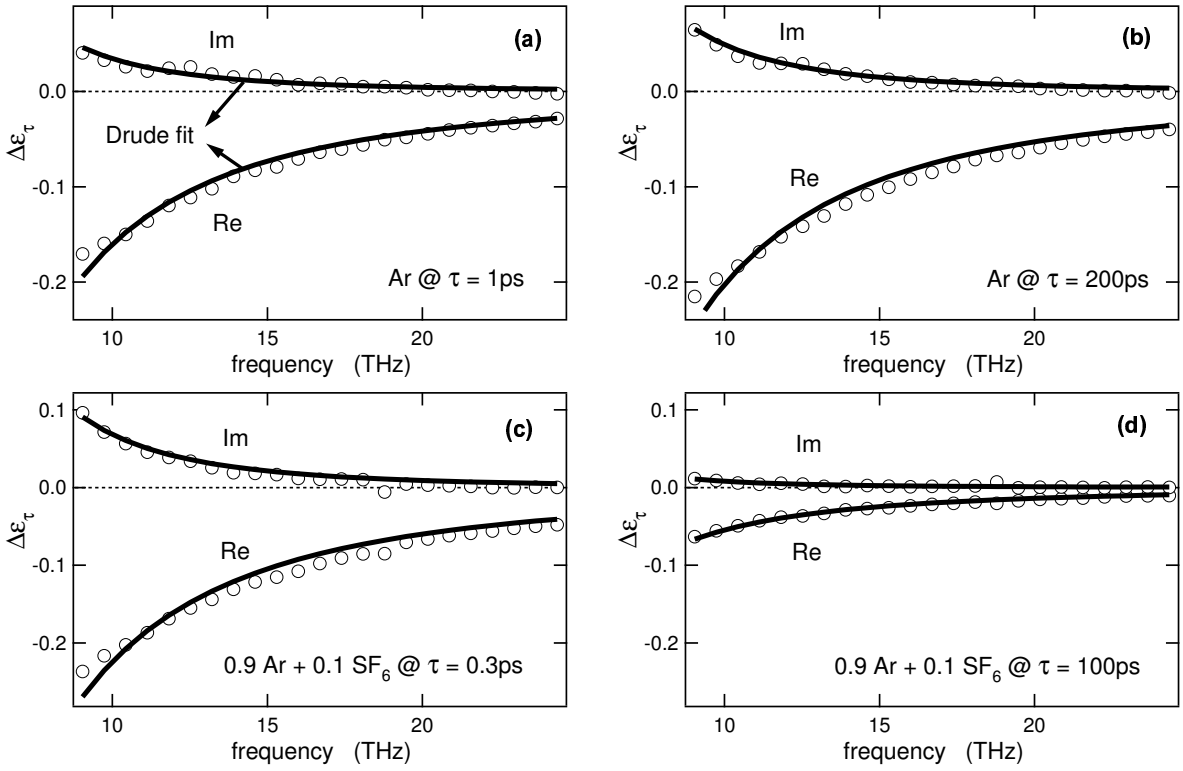

Figure 6.6.: Pump-induced changes $\Delta\varepsilon_\tau = \varepsilon_\tau - 1$ in the dielectric function. (a) $\Delta\varepsilon_\tau$ of Ar at $\tau = 1\,\mathrm{ps}$ after ionization. The Drude model excellently reproduces the experimental data. (b) Same as (a) at $\tau = 200\,\mathrm{ps}$. Note that the pump-induced changes have slightly increased. (c) $\Delta\varepsilon_\tau$ of the gas mixture $0.9\,\mathrm{Ar} + 0.1\,\mathrm{SF_6}$ at $\tau = 0.3\,\mathrm{ps}$ after ionization. The Drude model works fine also at this early delay. (d) Same as (c) at $\tau = 100\,\mathrm{ps}$. Note that the signal has already greatly reduced.

a laser-generated plasma channel in a N_2 gas jet and found a plasma expansion of $10\,\mu\mathrm{m}$ in 200 ps. However, this length should be considered as an upper limit of our experiment since their gas density was a factor of 100 lower than ours which greatly increases the mean free path and thus the plasma-expansion velocity. Moreover, their electron temperatures of $k_\mathrm{B}T_\mathrm{e} = 25\,\mathrm{eV}$ are larger than the temperatures of $k_\mathrm{B}T_\mathrm{e} \approx 2\,\mathrm{eV}$ suggested by our data (see below) which implies an increase of the electron velocity and the plasma-expansion velocity by another factor of 3 with respect to our experiments.

6.6. Results: Dynamics of the Free-Electron Density

The raw data are analyzed according to the procedure of the preceding section in order to obtain the dielectric function $\Delta\varepsilon_\tau(z = 0, \omega)$ in the center of the plasma. Figure 6.6 shows the pump-induced changes in the dielectric function of Ar and the gas mixture $0.9\,\mathrm{Ar} + 0.1\,\mathrm{SF_6}$ at various delays τ after excitation.

Upon excitation, the sample contains free electrons, ions, and neutral particles. As men-

tioned in Section 6.4, the free electrons are expected to make the dominating contribution to the THz response. Indeed, all real parts $\mathrm{Re}\,\Delta\varepsilon_\tau$ in Fig. 6.6 are negative, and their magnitude increases with decreasing frequency. According to Section 1.6.1, this is a clear signature of free charge carriers. Note that the real part $\mathrm{Re}\,(\Delta\varepsilon_\tau + 1)$ of the total dielectric function is always positive which excludes any complications of the anomalous skin effect as mentioned in Section 6.4.

Therefore, we employ the Drude formulas (1.12) and (1.13) to fit the measured dielectric function in which the fit parameters are the free-electron density n_e and the collision rate Γ of the free electrons. As seen in Fig. 6.6, the classical Drude model provides a nearly textbook-like reproduction of the experimental data. It should be emphasized that uncertainties of the exponents p_Re and p_Im of the data analysis in Section 6.5.3 lead to relatively moderate variations of the fit parameters n_e and Γ since p_Re and p_Im enter Eq. (6.8) in the radicand of the square root.

The temporal evolution of the fit parameters n_e and Γ is the main outcome of the preceding data analysis, and we start with a discussion of the dynamics of the density n_e of the free electrons.

6.6.1. Ar: Long-Lived Free Electrons

Figure 6.7(a) shows the temporal dynamics of the free-electron density n_e in the laser-ionized noble gas Ar. Note that n_e still increases during the first 50 ps after plasma generation and reaches a maximum of $n_\mathrm{e} = 2.5 \cdot 10^{17}\,\mathrm{cm}^{-3}$ which corresponds to 1 % of the total particle density of a gas under normal conditions. The additional generation of free electrons is most likely due to impact ionization of preexcited Ar atoms by fast electrons [Hol65]. After this increase, the electron density remains nearly constant up to $\tau = 200\,\mathrm{ps}$. These extremely long-lived electrons are typical for monatomic gases and are also observed for the noble gas Kr (data not shown). Although *binary* collisions are the most frequent interaction events they are very ineffective for the recombination of an Ar^+ ion with an electron e^- due to a lack of internal degrees of freedom: Apart from spontaneous photon emission there is no sink to absorb the kinetic and the binding energy of the electron. For this reason, the dominating recombination process is the *3-body* collision [Bul02, Hol65]

$$\mathrm{Ar}^+ + 2\,\mathrm{e}^- \longrightarrow \mathrm{Ar} + \mathrm{e}^-. \tag{6.9}$$

As a consequence, the rate equation for the electron population can be written as $\partial n_\mathrm{e}/\partial\tau = -K n_\mathrm{e}^3$ where equal densities of electrons and Ar^+ ions are assumed, $n_\mathrm{e} = [\mathrm{Ar}^+]$. The reaction constant of this reaction is given by the phenomenological relation $K = 4.2 \cdot 10^{-29} \cdot (T_\mathrm{e}/10000\,\mathrm{K})^{-8.29}\,\mathrm{cm}^6\,\mathrm{s}^{-1}$ [Bul02]. According to this formula and the slow electron decay found here, the electronic temperature must be significantly larger than 5000 K.

It should be mentioned that also sequential reactions like $\mathrm{Ar}^+ + 2\,\mathrm{Ar} \longrightarrow \mathrm{Ar}_2^+ + \mathrm{Ar}$, $\mathrm{Ar}_2^+ + \mathrm{e}^- \longrightarrow \mathrm{Ar} + \mathrm{Ar}^*$ can lead to an electron decay. However, $\partial n_\mathrm{e}/\partial\tau$ scales with n_e for

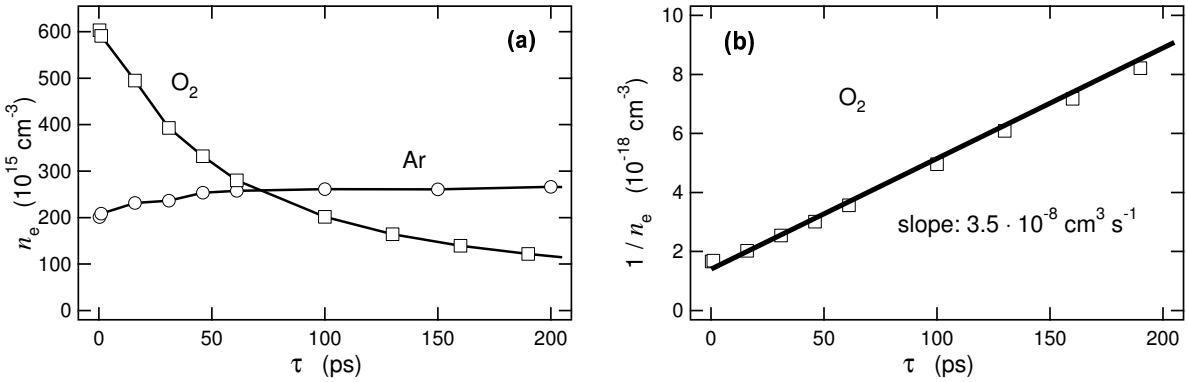

Figure 6.7.: (a) Temporal decay of the free-electron density n_e of laser-ionized gases of Ar and O_2. In Ar, n_e increases during the first 50 ps after excitation and remains constant afterwards. The electron decay in O_2 is much faster than in Ar as a consequence of the dissociative recombination (6.10) which does not occur in Ar. (b) The linear increase of the inverse electron density $1/n_e$ with time τ is a clear signature of the dissociative recombination in O_2.

this reactions instead of n_e^3. Therefore, the recombination reaction (6.9) is the dominating reaction at the elevated electron densities in our experiment [Bul02].

Before discussing the electron decay in O_2, we estimate the plasma parameters introduced in Section 6.2 for $n_e = 3 \cdot 10^{17}\,\mathrm{cm}^{-3}$ and $T_e = 10000\,\mathrm{K}$ which reflect the conditions in our laser-ionized gases. The electron degeneracy parameter of $\Theta \approx 500$ means that one can apply Maxwell-Boltzmann statistics. The electron-electron coupling parameter of $g_{ee} = 0.16$ indicates that the electron-electron interaction can still be considered as a perturbation of the free-electron gas. The Debye screening length amounts to $\lambda_D = 12\,\mathrm{nm}$ which is comparable to the mean distance $n_e^{-1/3} = 15\,\mathrm{nm}$ of adjacent electrons. The electron cooling proceeds very slowly as shown by the inverse Spitzer rate τ_{ei} of more than 1 ns.

6.6.2. O_2: Dissociative Recombination

Figure 6.7(a) shows that the free electrons in laser-excited O_2 decay much faster than in Ar, namely on a time scale of roughly 50 ps. The reason for this behavior are the internal excitations of the O_2^+ ion which can dissipate the kinetic and the binding energy of the recombining electron [Hol65]. This energy leads to a breaking of the O_2^+ bond in the so-called dissociative recombination [Hol65]

$$O_2^+ + e^- \longrightarrow O + O^*. \tag{6.10}$$

At least 1 of the oxygen atoms is in an excited state after this reaction.

The rate equation for this process is $\partial n_e/\partial\tau = -Kn_e^2$ if equal densities of electrons and O_2^+ ions are assumed, $n_e = [O_2^+]$. This yields the linear relationship

$$\frac{1}{n_e} = \frac{1}{n_e(0)} + K\tau$$

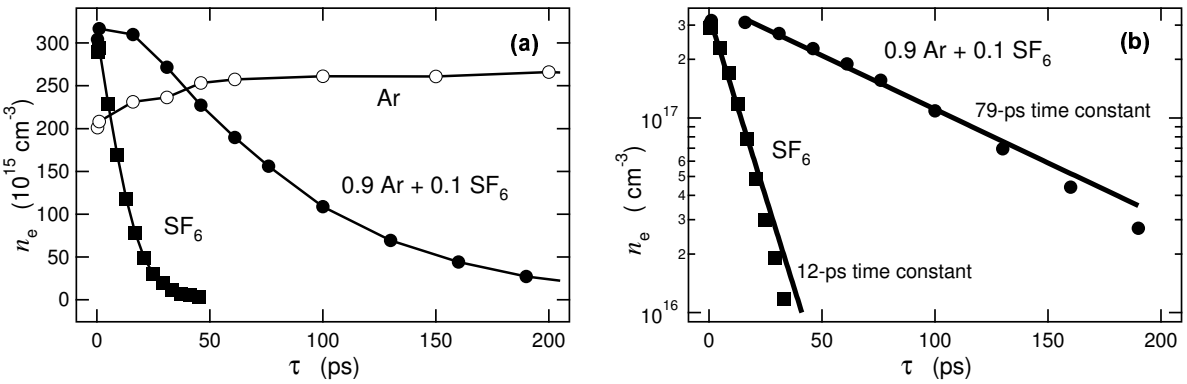

Figure 6.8.: (a) Temporal decay of the free-electron density n_e of laser-ionized SF_6 and the mixture $0.9\,\mathrm{Ar} + 0.1\,\mathrm{SF_6}$. The dynamics is much faster than in pure Ar. (b) Logarithmic plot of the dynamics in (a) together with monoexponential fits.

which indeed well reproduces the measured $1/n_\mathrm{e}$ vs. τ for a reaction constant of $K = 3.5 \cdot 10^{-8}\,\mathrm{cm^3\,s^{-1}}$ as can be seen in Fig. 6.7(b).

The same temporal behavior has been also observed on much longer time scales: For example, Mehr *et al.* ionized O_2 by microwave radiation and measured a linear increase of $1/n_\mathrm{e}$ with a temporal resolution of $\sim 1\,\mathrm{ms}$ [Meh69]. Similar to Ar, such experiments led to a phenomenological formula for the reaction constant $K = 2 \cdot 10^{-7} \cdot (T_\mathrm{e}/300\,\mathrm{K})^{-0.5}\,\mathrm{cm^3\,s^{-1}}$ as a function of electronic temperature T_e [Pet05]. The application of this formula to our K yields an electronic temperature of about $T_\mathrm{e} = 9000\,\mathrm{K}$. However, due to the uncertainty in the absolute values of n_e this value can be only considered as an estimate. The discussion of the free-electron decay in the remaining gases will permit a more accurate determination of the electronic temperature.

6.6.3. SF_6 in Ar: Electron Scavenger in Action

The man-made molecule SF_6 is known as a very effective electron scavenger due to its positive electron affinity of 1.1 eV and very large cross sections σ_att for electron attachment, see Fig. 6.9(a) [Chr00]. For these reasons and due to its chemical stability, it is used as insulating gas and arc interrupter in high-voltage devices. In order to study the influence of SF_6 on the lifetime of free electrons we add a small amount of SF_6 to the pure Ar gas.

Figure 6.8(a) shows that there is nearly no decay of the quasifree electrons in pure ionized Ar but this situation changes dramatically when we replace 10 % of the Ar by SF_6: Now the free-electron density decays *exponentially* with a time constant of 79 ps as demonstrated by the logarithmic plot in Fig. 6.8(b). Indeed, the attachment reaction

$$\mathrm{SF_6} + \mathrm{e^-} \longrightarrow \mathrm{SF_6^{-*}} \tag{6.11}$$

implies the rate equation $\partial n_\mathrm{e}/\partial\tau = -K \cdot [\mathrm{SF_6}] n_\mathrm{e}$ and thus a simple exponential decay

$$n_\mathrm{e}(\tau) = n_\mathrm{e}(0) \exp\left(-[\mathrm{SF_6}]\, K\tau\right) \tag{6.12}$$

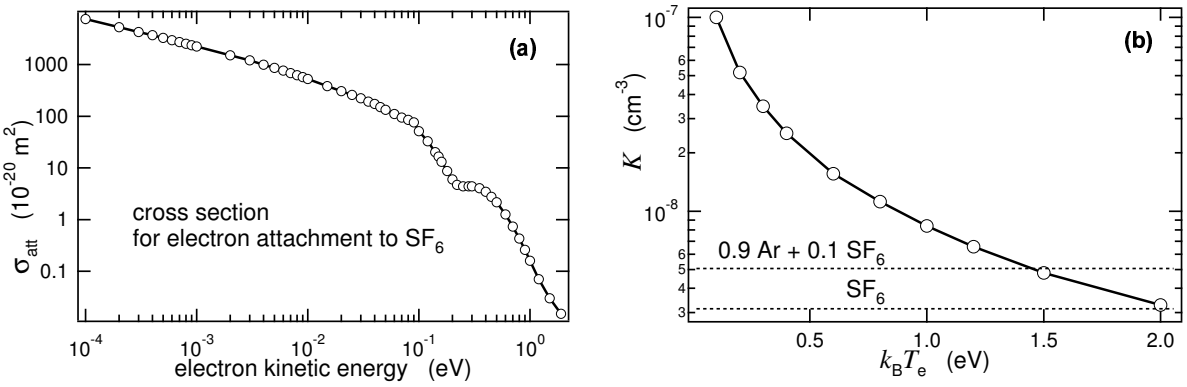

Figure 6.9.: (a) Total cross section σ_{att} for electron attachment to SF_6 as a function of the electron kinetic energy. Data are taken from Ref. [Chr00]. (b) Reaction constant K for electron attachment to SF_6 as a function of electronic temperature T_{e} according to Eq. (6.13). The 2 horizontal lines represent the measured reaction constants.

provided the reaction constant K and the number densities $[SF_6]$ and $[Ar^+]$ do not change in the course of the reaction.

The free-electron decay in *pure* SF_6 is shown in Fig. 6.8(a) and exhibits a time constant of 12 ps which is a factor of ≈ 7 faster than the decay in the Ar-SF_6 mixture. However, a factor of 10 is expected from the 10 times higher density of SF_6 molecules in the pure SF_6 gas, see Eq. (6.12). The slight difference between the observed and predicted time constant may be related to uncertainties of the SF_6 content in the Ar-SF_6 mixture, which is specified as $10 \pm 2\,\%$ by the supplier, and to different electron temperatures in the excited pure SF_6 gas and the mixture. Thus, we obtain values of $3.3 \cdot 10^{-9}$ and $5.1 \cdot 10^{-9}\,\mathrm{cm^3\,s^{-1}}$ for the reaction constant K in pure SF_6 and the Ar-SF_6 mixture, respectively.

To the best of my knowledge, direct measurements of the ultrafast free-electron decay induced by the electron scavenger SF_6 are performed here for the first time.

Estimate of the Electronic Temperature

The exponential decay (6.12) of the electron population in pure SF_6 and the mixture $0.9\,\mathrm{Ar} + 0.1\,SF_6$ permits to determine the corresponding time constants $[SF_6]\,K$ without knowing the absolute values of the electron density n_{e}. Therefore, the electronic temperature T_{e} can be determined with better accuracy than in the cases of Ar and O_2 provided a functional relationship between T_{e} and the reaction constant K is known. The latter can be derived with the aid of the cross section σ_{att} for electron attachment to SF_6 presented in Fig. 6.9(a). Note that σ_{att} strongly increases with decreasing kinetic energy of the electron. This fact also explains the increasing slope of the electron decay in the logarithmic plot of Fig. 6.8(b) when the electrons cool down in the course of time.

Similar to the considerations in Section 1.5.2, the change in the density $f(\boldsymbol{v}, t)$ of electrons

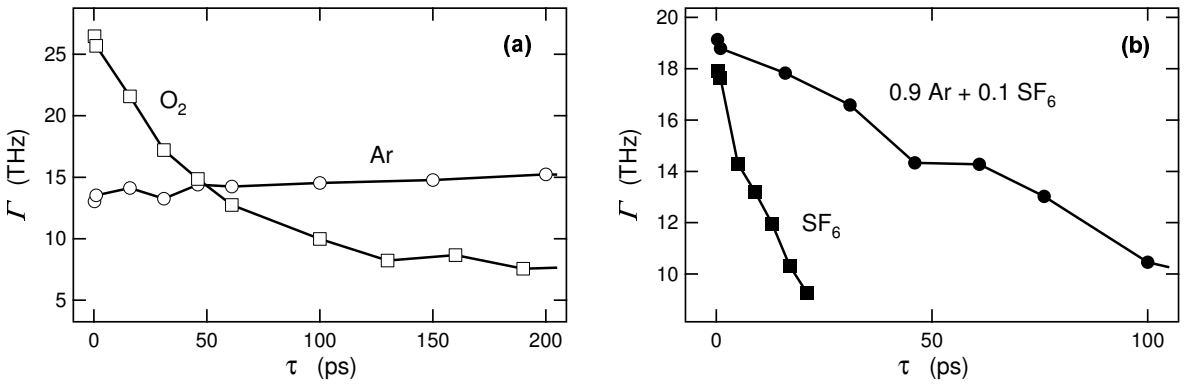

Figure 6.10.: (a) Temporal dynamics of the Drude collision rate Γ in laser-ionized Ar and O_2. (b) Same as (a) for pure SF_6 and the mixture $0.9\,Ar + 0.1\,SF_6$. Note that these dynamics resemble those of the free-electron densities in Figs. 6.7(a) and 6.8(a), respectively.

with a velocity within the interval $[\boldsymbol{v}, \boldsymbol{v} + \mathrm{d}\boldsymbol{v}]$ is given by

$$\frac{\partial f}{\partial \tau} = -[\mathrm{SF_6}]\sigma_{\mathrm{att}}|\boldsymbol{v}| \cdot f.$$

If f can be described by a Maxwell-Boltzmann distribution (1.14), the temporal change in the total electron density $n_\mathrm{e} = \int \mathrm{d}^3\boldsymbol{v}\, f$ is reduced to an integration over all kinetic energies ϵ of the electrons and yields the reaction constant [Jen01]

$$K = \frac{8\pi}{m_\mathrm{e}^2}\left(\frac{m_\mathrm{e}}{2\pi k_\mathrm{B} T_\mathrm{e}}\right)^{3/2} \int_0^\infty \mathrm{d}\epsilon\, \sigma_{\mathrm{att}}\, \epsilon \exp\left(-\frac{\epsilon}{k_\mathrm{B} T_\mathrm{e}}\right). \tag{6.13}$$

The derivation of this relation presumes a thermalized system of the free electrons.

The reaction constants K calculated in this way are plotted in Fig. 6.9(b) as a function of electronic temperature together with the constants measured in pure SF_6 and the Ar-SF_6 mixture. This graph allows to infer an electronic temperature T_e of 17000 to 23000 K which is of the same order of magnitude as the estimates based on the electron decay in Ar and O_2.

6.7. Results: Electron Collision Rate

We now discuss the Drude collision rate Γ of the free electrons whose temporal dynamics is plotted in Fig. 6.10 for all gases investigated. For example, the value $\Gamma \approx 15$ THz found for Ar implies a mean free path of roughly 30 nm for the electrons in this gas if their average kinetic energy is $k_\mathrm{B} \cdot 10000$ K. This mean free path is comparable to the approximate mean distance $n_\mathrm{e}^{-1/3} \approx 15$ nm of adjacent electrons or Ar^+ ions.

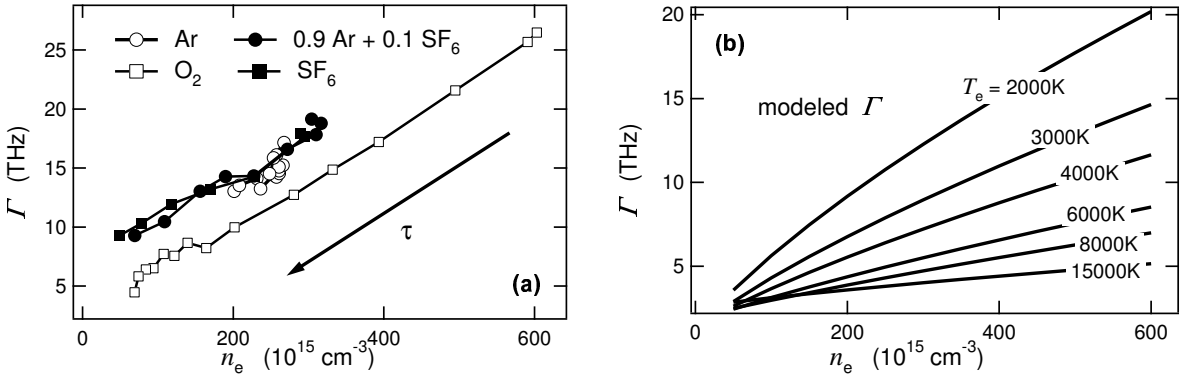

Figure 6.11.: (a) Plot of the collision rate Γ vs. the electron density n_e for all gases investigated. The temporal evolution is indicated by the arrow marked with "τ": A point $[n_e(\tau), \Gamma(\tau)]$ walks from the right to the left and from the top to the bottom of this diagram in the course of time. (b) Modeled Drude collision rates Γ as a function of electron density n_e and temperature T_e based on the procedure described in the text and Fig. 6.12. Note that the experimental values exceed those modeled by a factor of 3 for SF_6 and the Ar-SF_6 mixture.

Note that the evolution of the collision rate Γ in Fig. 6.10 is quite similar to that of the free-electron density in Figs. 6.7(a) and 6.8(a). This behavior appears most clearly for the fast free-electron decay in laser-excited SF_6 [Fig. 6.8(a)] and the corresponding decay of the collision rate [Fig. 6.10(b)]. For better comparison, Fig. 6.11(a) plots the collision rate Γ vs. the electron density n_e for *all* gases investigated and seems to reveal a nearly universal behavior: All curves have the same slope and, apart from that of O_2, even agree. This observation should not be overrated since the n_e axis involves some systematic error as mentioned in Section 6.6. Nevertheless, this graph clearly demonstrates that the collision rate Γ of the free electrons decreases with decreasing density n_e.

Within the framework of the Boltzmann approach to the dielectric function in Section 1.5.2, an increased collision rate is due to an increased number of scattering events of some "test electron" with other electrons (e), ions (i), and neutral particles (n). Since the number of neutral molecules remains virtually constant, the increase of Γ with n_e has to arise from e-e and e-i scattering.

Before modeling the dielectric function of our plasmas it should be mentioned that Mics *et al.* employed TRTS to measure the dielectric function of a cylindrical channel of ionized O_2 in the range from 1 to 3 THz [Mic05]. They found a scattering rate of 7 THz at an electron density of $1 \cdot 10^{16}\,\mathrm{cm}^{-3}$ which compares well to the data in Fig. 6.11(a).

6.7.1. Modeling the Dielectric Function

In order to estimate the contribution of e-i and e-n scattering to the dielectric function we now model the dielectric function of a partially ionized gas. We have to neglect e-e scattering such that Eq. (1.15) for the calculation of the dielectric function becomes

applicable. Rewriting this equation in terms of the electron kinetic energy $\epsilon = m_\mathrm{e}v^2/2$ instead of velocity v leads to

$$\varepsilon(\omega) - 1 = \left(\frac{2}{m_\mathrm{e}}\right)^{3/2} \frac{(4\pi e)^2}{3m_\mathrm{e}\omega} \int_0^\infty \mathrm{d}\epsilon \, \frac{\partial f}{\partial \epsilon} \epsilon^{3/2} \, \frac{1}{\omega + \mathrm{i}\gamma} \tag{6.14}$$

where f is the Maxwell-Boltzmann distribution (1.14). Since e-i and e-n scattering are considered as the relevant mechanisms for the current relaxation, Eq. (1.16) yields the collision rate

$$\gamma = v n_\mathrm{i} \sigma_\mathrm{ei} + v n_\mathrm{n} \sigma_\mathrm{en} \tag{6.15}$$

of electrons moving with velocity v. Note that γ is the collision rate of electrons moving with a velocity from a narrow interval $[v, v + \mathrm{d}v]$. It should not be confused with the Drude scattering rate Γ which to some extent can be understood as an average of γ since Eq. (6.14) involves an integration over *all kinetic energies* $\epsilon = m_\mathrm{e}v^2/2$ of the electrons.

We assume that there are only *positive* ions with a density n_i that equals the electron density, $n_\mathrm{i} = n_\mathrm{e}$. This implies a neutral-particle density of $n_\mathrm{n} = n_\mathrm{n0} - n_\mathrm{e}$ with $n_\mathrm{n0} = 2.5 \cdot 10^{19}\,\mathrm{cm}^{-3}$ being the particle density of a gas under ambient conditions. The approximate momentum-transfer cross section $\sigma_\mathrm{en} \approx 10^{-15}\,\mathrm{cm}^2$ for scattering between electrons and neutral atoms or small neutral molecules is taken from Ref. [Mit73].

Concerning the cross section σ_ei for e-i scattering, we assumed the screened Coulomb potential (6.1) to be the interaction potential between an electron and a positive ion. Dirk Gericke (Universität Greifswald) numerically solved the resulting 1-particle Schrödinger equation to provide us with the momentum-transfer cross sections σ_ei [Ger99]. This exact approach to the cross sections of the screened Coulomb potential is an improvement with respect to approaches involving the Born approximation [Sty02] or cut-off schemes [Ich73] which may lead to erroneous results [Sty02].

Figure 6.12 shows exemplary results of this modeling: The energy-dependent collision rate γ is plotted in Fig. 6.12(a) together with the weighting factor $\epsilon^{3/2}\partial f/\partial\epsilon$ of the integral (6.14) for an electron density of $3 \cdot 10^{17}\,\mathrm{cm}^{-3}$ and an electron temperature of 10000 K. Note that γ is large for electrons with kinetic energies below 0.5 eV. However, the weight of these scattering rates is small and rather peaks at about 1 eV where e-n scattering contributes already more than 40 % to the total collision rate of $\gamma \approx 5\,\mathrm{THz}$. Therefore one cannot expect an averaged scattering rate Γ much larger than 5 THz.

Figure 6.12(b) presents the resulting dielectric function for the same parameters $n_\mathrm{e} = 3 \cdot 10^{17}\,\mathrm{cm}^{-3}$ and $T_\mathrm{e} = 10000\,\mathrm{K}$. In order to get a direct comparison to the experimental data, we fit the modeled dielectric function (6.14) to the Drude formula (1.12). As seen in Fig. 6.12(b), the fit excellently reproduces the electron density which was used as an input of Eq. (6.14). We repeat this procedure over a wide range of electron densities n_e and temperatures T_e. The resulting Drude collision rates are plotted in Fig. 6.11(b) for comparison with the measured rates which is used as a basis of the following final discussion.

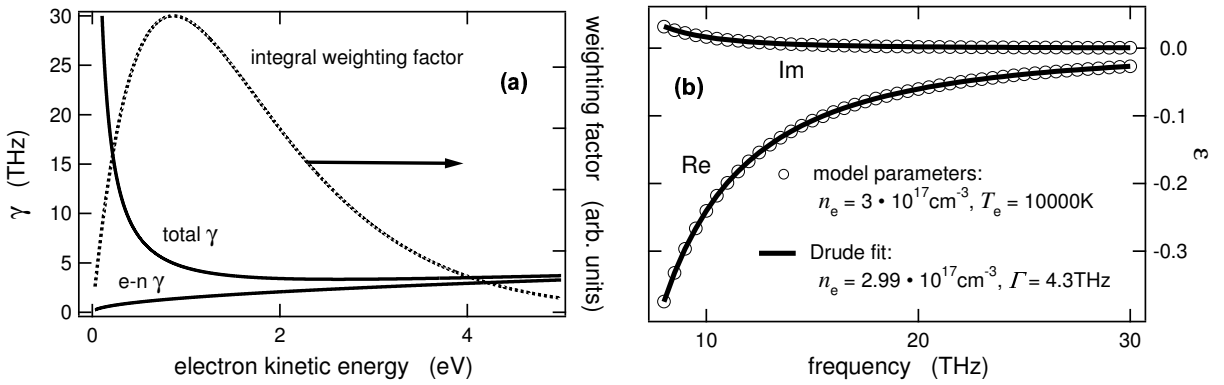

Figure 6.12.: (a) Collision rate γ for electrons with a kinetic energy ϵ together with the weighting factor $\epsilon^{3/2}\partial f/\partial\epsilon$ of the integral (6.14). Curves are calculated for an electron density of $3 \cdot 10^{17}\,\mathrm{cm}^{-3}$ and an electron temperature of 10000 K. Note that for $\epsilon > 1\,\mathrm{eV}$ e-n scattering more and more dominates the total scattering rate γ. (b) Dielectric function of a plasma calculated according to Eq. (6.14) for the same conditions as in (a). Thick solid lines mark a fit according to the Drude formula which excellently reproduces the input parameter $n_\mathrm{e} = 3 \cdot 10^{17}\,\mathrm{cm}^{-3}$.

6.7.2. Indication of Strong Electron-Electron Scattering?

Figure 6.11 shows that we only get agreement between the measured and modeled scattering rates when we assume an electronic temperature below 2000 K. Such a temperature seems very unlikely in view of the decay rates found in Section 6.6. This is especially true for SF_6 and the Ar-SF_6 mixture where the exponential decay of the free electrons convincingly indicated an electronic temperature of more than 15000 K. We conclude that the model for the dielectric function used in the last section greatly *underestimates* the electronic scattering rate by a factor of up to 5 for the case of SF_6.

The question arises whether e-i scattering really dominates the electron collision rate in our laser-ionized gases. There are 2 possible scenarios:

1. Electron-ion scattering is the major contribution to the electron collision rate Γ and is just underestimated by the model used in the preceding section. However, this assertion appears to be in contradiction to the dynamics of Γ in SF_6: In this gas, the attachment reaction (6.11) should result in a *decrease* of the electron density but in an *increase* of the number of negative ions SF_6^-. As a consequence of the increased number of scattering centers, Γ should also increase and lead to a curve of negative slope in Fig. 6.11(a).

   Such behavior is not observed and either indicates a strong contribution of e-e scattering to the Drude collision rate Γ or is due to a very efficient neutralization of the negative and positive ions by recombination reactions like

   $$SF_6^+ + SF_6^- \longrightarrow 2\,SF_6. \tag{6.16}$$

   In the most optimistic case, when adjacent positive and negative ions move directly towards each other, it takes about 10 ps to cover their mean initial distance of $n_\mathrm{e}^{-1/3} \approx$

15 nm such that a recombination can occur. This time is comparable to the 12-ps time constant of the free-electron decay in the SF_6 plasma and may explain why the Drude collision rate does not increase with decreasing n_e.

For the above estimate, the kinetic energy of the SF_6^- ion was set to the mean kinetic energy $k_B T_e \approx 2\,\text{eV}$ of the attached electron. Taking the Coulomb attraction between the ions into account does not substantially shorten the recombination time. Nevertheless, more thorough approaches are required to calculate the neutralization rate of positive and negative ions in reactions like (6.16) which for example also account for the occurrence of ion fragments such as SF_5^- [Chr00].

2. In the 2nd scenario, e-e scattering is assumed to make the major contribution to the electron collision rate Γ. Such a scenario would immediately explain why the modeled rates Γ in Fig. 6.11 are substantially lower than those observed: Electron-electron interaction is simply not included in this model.

   In literature [Sty02], e-e scattering is usually considered as a minor contribution to the velocity relaxation of the electrons based on an argument similar to that in Section 1.7: A collision between 2 electrons, for example shown in Fig. 1.3, involves the conservation of the total momentum $m_e \boldsymbol{v}_1 + m_e \boldsymbol{v}_2$ of the 2 electrons; as a consequence, the electronic current does not change, either.

   However, e-e scattering can become operative in the current relaxation when higher-order processes are considered [Sty02, Ger05]: For example, 2 electrons from a Maxwell-Boltzmann distribution with comparable velocities scatter with each other resulting in the velocities v_1 and v_2. In case of $v_1 \ll v_2$, the electron with velocity v_1 suffers a much larger collision rate with ions as seen in Fig. 6.12. This is not compensated for by the electron with the large velocity. As is known from calculations of the dc conductivity of plasmas, this effect can make up to 40 % of the contribution of e-i scattering to the current relaxation [Sty02]. This is still not enough to explain the discrepancy between the curves in Fig. 6.11(a) and Fig. 6.11(b) for electron temperatures of about 15000 K. Improved calculations of the ac conductivity may have to include, for example, dynamical screening effects which are not yet accounted for by the static Debye screening of Eq. (6.1) [Rei00].

We conclude that the present arguments are not sufficient to decide which of the 2 scenarios corresponds to reality. If the 1st scenario is true, the Drude collision rate Γ represents a measure of the ion density making time-resolved THz spectroscopy an easy-to-interpret and useful tool to study the dynamics of optically excited gases.

6.8. Conclusion and Outlook

In conclusion, we employed time-resolved THz spectroscopy to study the electron dynamics in optically ionized gaseous Ar, O_2, SF_6, and the gas mixture $0.9\,\text{Ar}+0.1\,SF_6$. The measured

transient dielectric function allows for an excellent description by the simple Drude model leading to the temporal dynamics of the free-electron density n_e and the Drude collision rate Γ. The electrons in Ar decay much slower than in O_2 due to a lacking dissipation channel for the kinetic and binding energy of the electron. However, the decay can be accelerated enormously by adding the electron scavenger SF_6 to Ar. In pure SF_6, the free-electron decay occurs with a time constant as short as 12 ps which directly demonstrates the ultrafast extinction of free electrons in SF_6 and allowed for a quite reliable estimate of the electronic temperature of 17000 to 23000 K. The Drude scattering rate Γ was found to increase with the electron density. Assuming only collisions between electrons and ions and electrons and neutral particles underestimates the measured rates significantly. This and the fact that the electron attachment does not result in an temporal increase of Γ might point to a dominant contribution of electron-electron scattering to the current relaxation.

Future work requires a more thorough modeling of the dielectric function of optically ionized gases in the THz range. The same applies to the recombination of positive and negative ions in SF_6. Regarding the experimental setup, the somewhat unknown sample structure could be improved by employing a supersonic gas jet in a small vacuum chamber. Then one deals with a thin and homogeneous gas film and can both pump and probe the sample from the same side. The resulting increased temporal resolution may be used to look for effects in the early stage after plasma generation. An example is the build-up of the screening in an initially uncorrelated plasma which was already observed in optically excited semiconductors [Hub01].